Chinese Chemical Letters 35 (2024) 109892

Contents lists available at ScienceDirect

Chinese Chemical Letters

journal homepage: www.elsevier.com/locate/cclet

Killing two birds with one stone: Enhancing the photoelectrochemical water splitting activity and stability of $BiVO_4$ by Fe ions association

Hailang Deng[a], Abebe Reda Woldu[a], Abdul Qayum[a], Zanling Huang[a], Weiwei Zhu[b,f,*], Xiang Peng[c], Paul K. Chu[e], Liangsheng Hu[a,d]

[a] Department of Chemistry and Key Laboratory for Preparation and Application of Ordered Structural Materials of Guangdong Province, Shantou University, Shantou 515063, China
[b] Department of Mechanical Engineering, Shantou University, Guangdong 515063, China
[c] Hubei Key Laboratory of Plasma Chemistry and Advanced Materials, School of Materials Science and Engineering, Wuhan Institute of Technology, Wuhan 430205, China
[d] Chemistry and Chemical Engineering Guangdong Laboratory, Shantou 515063, China
[e] Department of Physics, Department of Materials Science and Engineering, and Department of Biomedical Engineering, City University of Hong Kong, Hong Kong, China
[f] Shantou Huaxing Metallurgical Equipment Co., Ltd., Shantou 515063, China

ARTICLE INFO

Article history:
Received 8 February 2024
Revised 15 April 2024
Accepted 15 April 2024
Available online 16 April 2024

Keywords:
Photoelectrochemical water splitting
$BiVO_4$ photoanodes
Fe(III) ions
Oxygen evolution reaction
Dynamic changes

ABSTRACT

$BiVO_4$ is a promising semiconducting photoanode for photoelectrochemical (PEC) water splitting due to its suitable bandgap. However, the dissolution of V^{5+} and sluggish reaction kinetics at the surface in the oxygen evolution reaction (OER) limit its applications. Herein, we report a convenient strategy to change the microenvironment by adding Fe(III) into the electrolyte. During the PEC process, Fe(III) ions not only improve the current density, but also show excellent stability toward $BiVO_4$. Consequently, the current increases by more than 1.7 times compared to that without Fe(III). Photoelectrochemical, morphological, and structural characterizations reveal that the FeOOH co-catalyst produced *in situ* on the $BiVO_4$ photoanode by cyclical formation of the intermediates at the electrode/electrolyte interface during OER accelerates the OER kinetics and prevents photo-corrosion by suppressing the dissolution of V^{5+}. The results reveal a new strategy for the multifunctional modification of photoanodes for efficient solar conversion.

Photoelectrochemical (PEC) water splitting is one of the promising strategies to convert solar light into hydrogen to meet the increasing demand for clean energy from renewable sources [1–3]. Although hydrogen is produced from water by the hydrogen evolution reaction (HER) on the cathode, usually a Pt-based electrode [4], the oxygen evolution reaction (OER) on the photoanode is the rate-determining step in PEC water splitting, but this process is sluggish due to the multiple proton-coupled electron transfer [1,5]. Therefore, it is crucial to design and prepare efficient photoanodes with sufficient light absorption, effective charge separation, and fast reaction kinetics for OER [6–8]. Among the different materials, nanostructured bismuth vanadate ($BiVO_4$) has attracted much attention due to its suitable bandgap (~2.4 eV), low cost, and facile synthesis [9–14]. Nevertheless, its low carrier mobility and short hole diffusion length cause serious bulk and surface electron–hole recombination [15], which causes photo-corrosion of $BiVO_4$, loss of V^{5+}, and poor long-term stability [14,16-18]. Doping [19–21], facet tailoring [22–24], and oxygen vacancies construction [15,25-27], have been proposed to overcome the transport limitation and enhance the separation of charge carriers. In addition, coatings made of oxygen evolution catalysts (OECs) and surface passivation layers have been suggested to inhibit the loss of V^{5+} and improve the OER activity [9,28-30].

Among the different types of OECs, VIII metal (Fe, Co, Ni)-based oxides and/or (oxy)hydroxides, especially FeOOH, have attracted interest in recent years [9,31-35]. The Bi–O–Fe interfacial bonds have been observed to be the active sites for the enhanced OER activity and the suppressed dissolution of V^{5+} in turn improves the PEC stability [32]. For example, Zhang *et al.* have prepared ultrathin and crystalline β-FeOOH on $BiVO_4$ photoanodes, which exhibit remarkable photocurrents because the ultrathin structure of FeOOH exposes more active sites to accelerate the reaction kinetics [33]. However, it is challenging to cover $BiVO_4$ crystals completely unless a sufficiently thick layer is deposited, but a thick OECs/protector causes unnecessary parasitic light absorption and may compromise the PEC performance of $BiVO_4$ [2]. Moreover,

* Corresponding author.
E-mail address: wwzhu@stu.edu.cn (W. Zhu).

https://doi.org/10.1016/j.cclet.2024.109892
1001-8417/

the surface structure changes under strong alkaline conditions at a high anodic potential consequently hurting the durability [36]. Hence, uniform and conformal deposition of FeOOH with a suitable thickness on $BiVO_4$ with large aspect ratios remains challenging.

The composition of electrolytes and modulation of the catalytic environment have gained more recent attention because there is a dynamic ion exchange process between the electrocatalysts and electrolytes, especially in electrochemical cycling [11,37-39]. For example, Lee and Choi have used a V^{5+}-saturated electrolyte to inhibit the loss of V^{5+} from the $BiVO_4$ lattice by dissolution consequently suppressing photo-corrosion during solar water splitting and increasing the photostability of $BiVO_4$ [11]. Nevertheless, the addition of V^{5+} to the electrolyte cannot boost the OER kinetics. Our recent study reveals that Fe(III) ions can serve as the dynamic sites to promote the OER activity and long-term stability by cyclical formation of the intermediates on the electrode/electrolyte interface and *in situ* growth of FeOOH on the surface of the electrode [40,41].

Herein, a convenient strategy to simultaneously overcome the sluggish reaction kinetics and poor stability of $BiVO_4$ is described by incorporating Fe(III) cations into the electrolyte. During OER, the Fe(III)-containing electrolyte shows dynamic changes between Fe(III) and FeOOH (Fe(III) → Fe^{x+} → Fe–OH → Fe–O → FeOOH → Fe(III)) accompanying with FeOOH co-catalyst produced *in situ* on the $BiVO_4$ photoanode (Scheme 1). The $BiVO_4$/FeOOH photoanode shows a current density of 2.21 mA/cm^2 at 1.23 V (*vs.* RHE) under AM 1.5G illumination (100 mW/cm^2), which is considerably higher than that of the pristine $BiVO_4$ (1.29 mA/cm^2). The excellent PEC properties stem from the *in situ* generated FeOOH on the surface, which, as the active sites, accelerates oxygen evolution. Furthermore, the PEC stability of the $BiVO_4$/FeOOH is enhanced due to the *in situ* formed FeOOH that prevents the corrosion of the photoanode by suppressing the dissolution of V^{5+}. The results reveal a facile, cost-effective, and efficient strategy for efficient and stable PEC systems.

The PEC water oxidation properties of the $BiVO_4$ photoanodes are determined under AM 1.5G illumination, and the current density curves are shown in Fig. 1. Various concentrations of Fe(III) ions are added to the KBi electrolyte to examine the effects on the PEC activity. As shown in Fig. S1 (Supporting information), Fe(III) ions in the electrolyte dramatically enhances the current densities. The maximum current density of 2.21 mA/cm^2 is achieved at an onset potential of 0.40 V by adding 1 mmol/L Fe(III) to the electrolyte (KBi + Fe(III)). Fig. 1a shows the instantaneous current density curves of the $BiVO_4$ photoanodes in the KBi and KBi + Fe(III) electrolytes. In both electrolytes, the dark current densities are negligible, indicating that Fe(III) ions do not take part in the redox reaction for OER at below 1.23 V. To explore the stability of the photoanodes, the *i-t* curves are acquired at 1.23 V. As shown in Fig. 1b, the photoanode shows a rapid decrease in the current

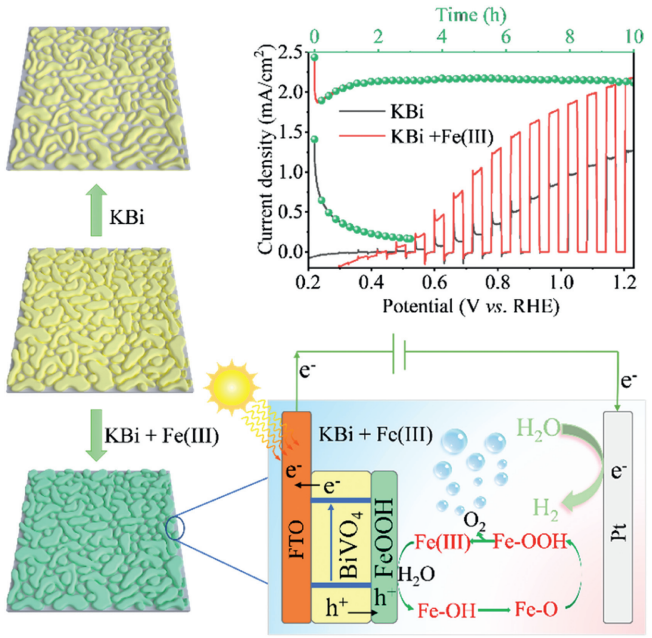

Scheme 1. Schematic illustration of the $BiVO_4$ photoanodes in KBi and KBi + Fe(III).

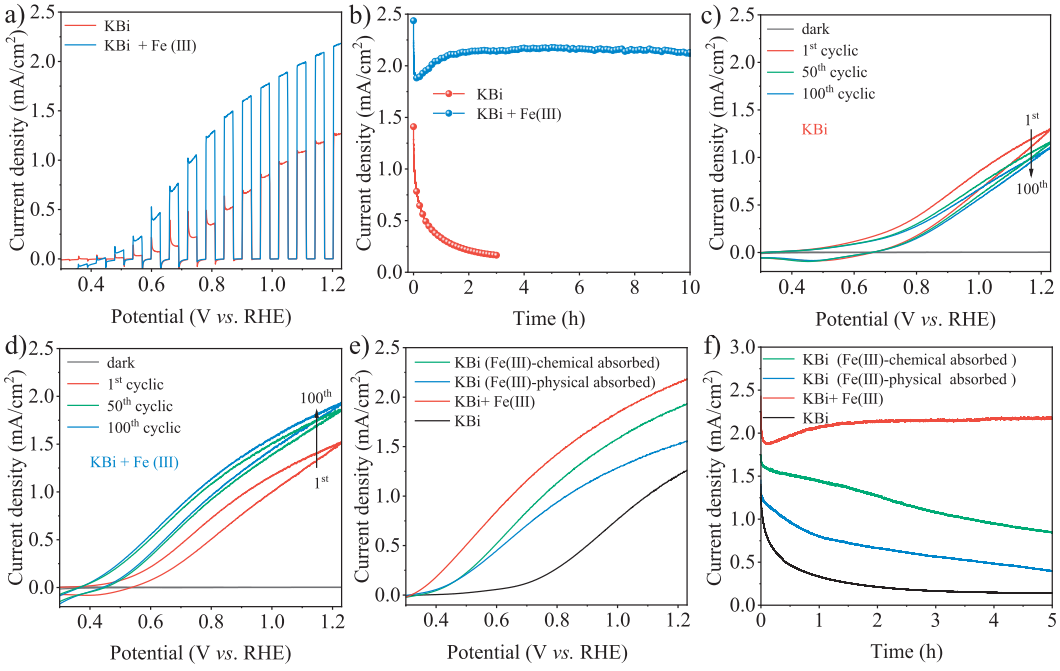

Fig. 1. (a) Chopped illumination curves. (b) Photostability of $BiVO_4$ photoanodes in KBi and KBi + Fe(III). CV measurements of the $BiVO_4$ photoanodes in (c) KBi and (d) KBi + Fe(III). (e) LSV and (f) *i-t* curves of the photoanodes for different pretreatment of Fe(III).

densities in the KBi electrolyte from about 1.41 mA/cm^2 at the beginning to 0.1 mA/cm^2 after 3 h indicative of serious photo-corrosion and V^{5+} dissolution from the crystal lattice [1,11]. Remarkably, the photoanode displays a different trend if Fe(III) ions are added to the solution (KBi + Fe(III)). The current densities increase in the first 1 h perhaps due to the redox process of Fe(III) and deposition of FeOOH on the surface of the photoanode [40–42]. After 1 h, the current density plateaus at 2.21 mA/cm^2 and remains steady for over 10 h, consistent with the LSV results in Fig. S2a (Supporting information). The *i-t* curves of FTO without $BiVO_4$ obtained from the KBi + Fe(III) solution under light illumination exhibit negligible current densities (Fig. S2b in Supporting information), indicating that the Fe species are unable to generate photogenerated charge carriers in OER. Inductively coupled plasma (ICP) spectroscopy was used to analyze the electrolyte after 3 h of *i-t* measurement. The results show the presence of V in both the KBi and KBi + Fe(III) electrolytes (Fig. S3 in Supporting information), indicating the dissolution of V in both systems. However, the concentration of V in KBi (78.35 μg/L) is significantly higher than that of the KBi + Fe(III) (41.32 μg/L), suggesting the role of Fe(III) in suppressing the dissolution of V that ultimately prevents the $BiVO_4$ photoanode from photo-corrosion. These results indicate that the Fe species plays the role of a co-catalyst in the $BiVO_4$ photoanode to improve both the PEC activity and stability. The PEC performance of our system reaches and even outperforms most recent photoelectrocatalysts based on OECs decorated $BiVO_4$ electrodes (Table S1 in Supporting information), while our method is much more convenient.

The Fe(III) catalytic mechanism is explored. CV is performed on the $BiVO_4$ photoanode in 1.0 mol/L KBi with and without Fe(III) addition. As shown in Fig. 1c, the current densities decrease with CV cycles in KBi, implying gradual inactivation of the $BiVO_4$ photoanode. In contrast, the current densities increase gradually in KBi + Fe(III) as shown in Fig. 1d. During CV, the photoanode is cycled between the PEC active and inactive states. The catalyst/electrolyte interface undergoes dynamic changes during PEC, leading to Fe incorporation into the photoanode [43]. To verify the photocurrent of $BiVO_4$ photocurrent has stabilized, the different CV (1^{st}, 50^{th}, 80^{th}, and 100^{th}) cycles has been carried out as shown in Fig. S4 (Supporting information). The 80^{th} and 100^{th} photocurrent density indicate almost the same, suggesting that 100 cycle is enough for supper saturation of the photocurrent. To confirm that Fe is incorporated into the photoanode rather than absorbing on the surface, we compare the PEC activity of the $BiVO_4$ photoanodes in KBi and KBi + Fe(III), Fe(III)-chemical absorbed (activated by CV cycles in KBi + Fe(III)) in KBi, and Fe(III)-physical absorbed (immersed in KBi + Fe(III) for the same time as that of CV-activated sample) in KBi. As shown in Fig. 1e, the Fe(III)-chemical absorbed and Fe(III)-physical absorbed photoanodes display higher current densities than the fresh photoanode in KBi, indicating that Fe(III) is vital to improving the PEC activity. Moreover, the photoanode in KBi + Fe(III) shows higher current densities than the Fe(III)-physical absorbed photoanode in KBi, confirming the incorporation of Fe(III) into the photoanode during PEC rather than absorption. In addition, the Fe(III)- chemical absorbed anode in KBi exhibited lower activity than that of the photoanode tested in KBi + Fe(III), ascribing that Fe(III) availability is the key to maintaining the PEC activity, which is further confirmed by the *i-t* curves in Fig. 1f. To verify the advantages of the proposed strategy, FeOOH is deposited on the surface of the $BiVO_4$ photoanode ($FeOOH/BiVO_4$) by photo-deposition using a method reported by Choi *et al.* [34] and compared its performance with the $BiVO_4$ photoanode. As shown in Fig. S5 (Supporting information), the current densities of $FeOOH/BiVO_4$ tested in KBi and $BiVO_4$ tested in KBi + Fe(III) are comparable (Fig. S5a) while the $FeOOH/BiVO_4$ presents a poor stability (Fig. S5b).

The applied bias potential efficiency (ABPE) is measured in KBi and KBi + Fe(III) and the maximum ABPEs are calculated to be 0.18% (0.92) and 0.55% (0.82), respectively (Fig. 2a), confirming that the addition of Fe(III) to the electrolyte can enhance the catalytic ability in water oxidation [44]. Fig. 2b and Fig. S6 (Supporting information) show the interfacial charge transfer (η_{trans}) efficiency of the water oxidation reaction. In the electrolyte without Fe(III), the photoanode exhibits a very low efficiency of 29.1% at 1.23 V, but adding Fe(III) increases the η_{trans} efficiency to 62.65%. Fig. 2c shows the EIS data to further elucidate the interfacial charge

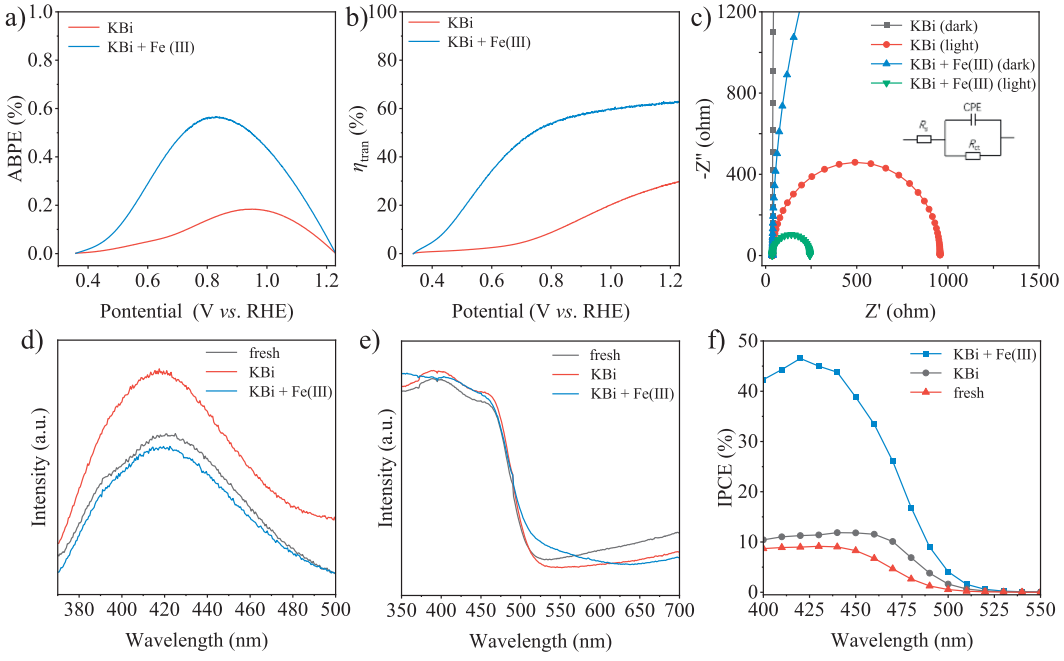

Fig. 2. (a) ABPE, (b) charge transfer efficiency, (c) Nyquist plots at 0.8 V under illumination or in the dark for the $BiVO_4$ photoanodes with or without Fe^{3+}. (d) PL spectra, (e) UV–vis absorption spectra, and (f) IPCE at 1.23 V of $BiVO_4$ photoanodes after the *i-t* test in KBi or KBi + Fe(III).

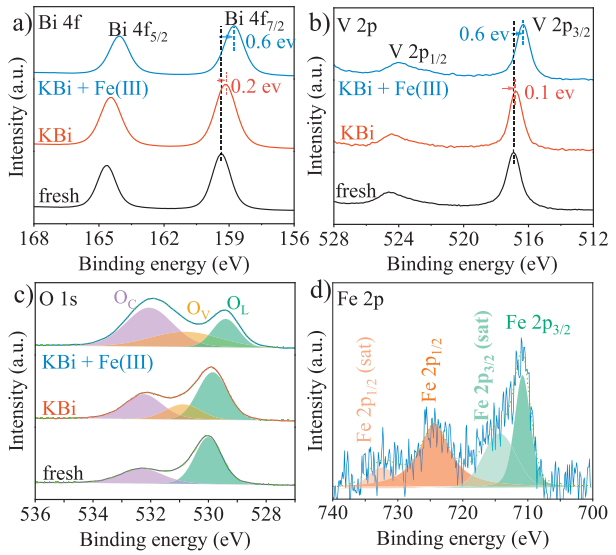

Fig. 3. XPS spectra of (a) Bi 4f, (b) V 2p, and (c) O 1s of the pristine $BiVO_4$ photoanodes before and after the *i-t* test with or without Fe(III). (d) Fe 2p of the photoanode after the *i-t* test with Fe(III).

transfer and oxygen evolution kinetics. The curvature diameter of the photoanodes in KBi + Fe(III) under illumination is the smallest among the samples, providing evidence that Fe(III) improves the charge transfer between the photoanode and electrolyte [45].

Photoluminescence (PL) is monitored to determine the electron-hole recombination rates [46]. As shown in Fig. 2d, all the photoanodes show the maximum intensity at about 420 nm. The photoanode after the *i-t* test in KBi exhibits stronger intensity than the fresh one, demonstrating higher electron-hole recombination rates. However, after the *i-t* test in KBi + Fe(III), the PL peak intensity declines, implying smaller electron-hole recombination ratios compared with other photoanodes. The results demonstrate that addition of Fe(III) to the electrolyte improves the separation efficiency of photo-generated carriers [1,47]. As revealed by the UV–vis diffuse (Fig. 2e), the absorptance does not change significantly. All the photoanodes exhibit a light absorption edge at ~500 nm, corresponding to a bandgap of about 2.40 eV (Fig. S7a in Supporting information). After Fe incorporation, the photoanodes show a similar light absorption edge and bandgap compared to the fresh one, indicating that the Fe species do not affect the bandgap and the light absorption properties of the $BiVO_4$ photoanodes [48]. There is a slight shift in absorption edges of the $BiVO_4$ photoanodes after the *i-t* test in KBi + Fe(III) (Fig. S8 in Supporting information), attributing to the formation of FeOOH on the surface of the photoanode. The PEC performance at different incident lights is studied using the IPCE curves of the different photoanodes. As shown in Fig. 2f, all the photoanodes have IPCE values of less than 500 nm, consistent with the UV–vis light absorption curves. The IPCE values of the fresh photoanode and photoanode after the *i-t* test in KBi and KBi + Fe(III) at 420 nm are 11.27%, 8.98%, and 46.53%, respectively. To get more insights into the electronic properties, Mott-Schottky (MS) curves are acquired in KBi without illumination. As shown in Fig. S7b (Supporting information), all the samples exhibit the n-type semiconductor behavior. Therefore, the above experiments confirm that the incorporation of Fe(III) improves the charge transfer kinetics rather than changing the band structure.

The effects of Fe incorporation on the surface chemical states and electronic structures of the photoanodes are examined by XPS (Fig. 3 and Fig. S9 in Supporting information). The survey XPS spectra of the prepared $BiVO_4$ photoanodes reveal the existence of Bi, V, and O elements. From the high-resolution XPS spectra, the peaks at about 159.0 and 164.7 eV are attributed to Bi^{3+} of Bi 4f (Fig. 3a). The two peaks at about 516.9 and 524.5 eV are ascribed to the V $2p_{3/2}$ and V $2p_{1/2}$ states, respectively, indicative of the V^{5+} characteristics (Figs. 3a and b) [49]. The XPS peaks of O 1s can be divided into lattice oxygen (O_L), oxygen vacancy (O_V), and chemically adsorbed or dissociated oxygen species (O_C) from water molecules, respectively (Fig. 3c) [50,51]. It is worth noting that the XPS spectra of Bi 4f and V 2p after the *i-t* test in KBi + Fe(III) show a shift toward lower binding energies, suggesting that the interaction between Fe species and $BiVO_4$ produces excellent electron transport [29]. Furthermore, the chemical shift of O_L decreases after the *i-t* test in KBi + Fe(III), indicating oxygen vacancies and bigger electron densities around the Bi and V atoms. The peaks at 711.0 and 724.3 eV can be ascribed to Fe $2p_{3/2}$ and Fe $2p_{1/2}$, and those at 713.8 and 734.3 eV are typical satellite (Sat.) peaks (Fig. 3d). The XPS survey spectra corroborate successful incorporation of Fe species into the photoanodes.

To better understand the roles of Fe species, SEM, XRD, TEM, and Raman scattering are performed. As shown in Fig. 4a, the SEM image exhibits irregular nanoparticles with a length of about 220 nm. The initial nanopores in the films expand and are interconnected with each other to form a three-dimensional (3D) nanoporous structure, which benefits the interactions between the photoanodes and electrolytes. The stability evaluation in KBi shows that the $BiVO_4$ structure is destroyed and the density of nanopores is less than that of the fresh one (Fig. 4b) reflecting dissolution of $BiVO_4$. However, the surface of the photoanode tested in KBi + Fe(III) retains the original structure but becomes roughing, indicating that the photoanodes can be protected from photo-corrosion by the Fe species during PEC (Fig. 4c).

The XRD patterns (Fig. S10 in Supporting information) of the $BiVO_4$ photoanodes show monoclinic $BiVO_4$ (JCPDS No. 14–688) and the FTO substrate [52]. No additional diffraction peaks can be detected after the *i-t* test in KBi + Fe(III), maybe due to the small concentration of the Fe(III) species [44]. As shown in Fig. S11 (Supporting information), the main Raman peaks at 327 and 369 cm^{-1} correspond to the asymmetric and symmetric deformation modes of the VO_4^{3-} tetrahedron [53]. The peaks at 713 and 829 cm^{-1} arise from the asymmetric and symmetric stretching modes of the V–O bond [54]. After the *i-t* test in KBi + Fe(III), the photoanodes show the typical peaks at ~447 and 609 cm^{-1} related to the Fe–O–Fe and Fe–O vibrational mode of FeOOH, respectively [55,56]. Compared to the pristine $BiVO_4$ photoanode, the photoanode after the *i-t* test in KBi + Fe(III) shows a negative shift and broader peak for the symmetric stretching of V–O (829 cm^{-1}) implying that FeOOH weakens the lattice structure of $BiVO_4$ [57]. Interestingly, the peak intensity obtained after the *i-t* test in KBi + Fe(III) decreases subtly in comparison with the fresh sample, while the intensity of the photoanode declines noticeably after the *i-t* test in KBi, which further confirms that the Fe species can prevent photoanodes from photo-corrosion. Raman scattering shows that FeOOH is loaded onto the surface of $BiVO_4$ photoanode during PEC. TEM conducted on the pristine photoanode shows lattice fringes of 0.308 nm corresponding to the (−121) faces of $BiVO_4$ (Fig. 4d), consistent with the XRD. The HR-TEM image after the *i-t* test in KBi + Fe(III) reveals *in situ* generation of ultrathin FeOOH with a thickness of ~5 nm on the monoclinic $BiVO_4$ photoanode (Fig. 4e). Fig. 4f shows a lattice fringe of 0.254 nm corresponding to the (101) face of FeOOH and the EDS elemental maps disclose uniform distributions of Bi, V, and Fe (Fig. 4g).

Based on the above data, the FeOOH/$BiVO_4$ heterostructure is formed after the *i-t* test. The current densities do not change with *i-t* testing time. The FeOOH/$BiVO_4$ heterostructure may be formed *in situ* even after a short time and Fe(III) boosts the OER kinetics by cyclic formation of intermediates at the photoelectrode/electrolyte interface, so the Fe(III)-containing atmosphere is dynamic to

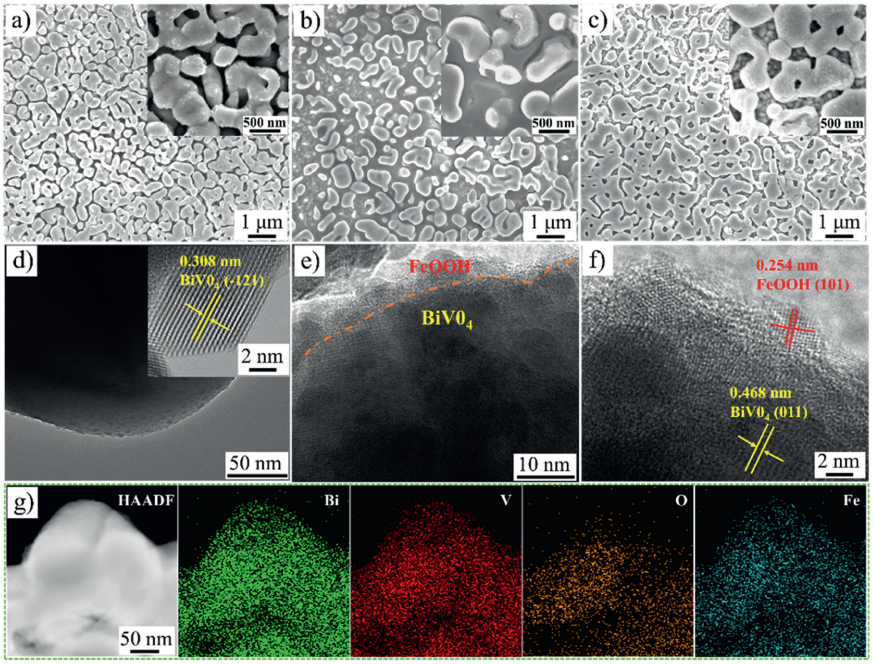

Fig. 4. SEM images of (a) pristine $BiVO_4$ photoanodes, (b) after 5-h *i-t* test without Fe(III), and (c) after *i-t* test with Fe(III). (d) TEM images of pristine $BiVO_4$ photoanode. (e, f) $BiVO_4$ photoanode after the *i-t* test with Fe(III). (g) HAADF-STEM image and elemental maps of the $BiVO_4$ photoanode after the 10-h *i-t* test with Fe(III). The insets in (a-d) are the corresponding high-magnification images.

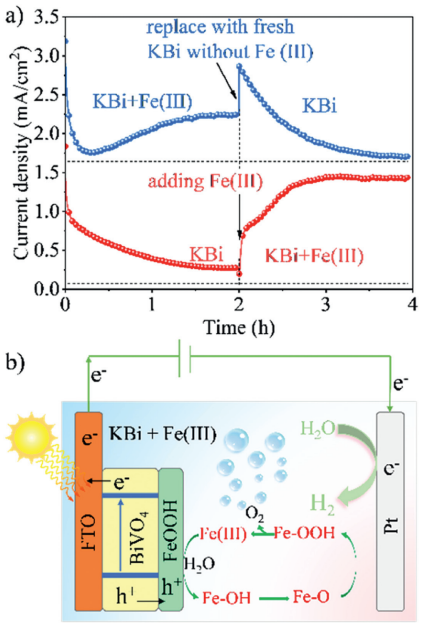

Fig. 5. (a) *i-t* plots of the $BiVO_4$ photoanodes in KBi and KBi + Fe(III). (b) Proposed mechanism of Fe(III) ions enhanced PEC water splitting.

preserve the photo-stability of the system. The PEC stability of the $BiVO_4$ photoelectrodes is investigated in KBi and KBi + Fe(III). As expected, the photoanode shows obvious decline in the current densities in KBi (Fig. 5a, red plots). After adding Fe(III) ions, the current density increases and remains stable at 1.43 mA/cm^2 rather than 2.21 mA/cm^2, suggesting partial dissolution of $BiVO_4$ and that the Fe species can prevent the photoanode from further photo-corrosion. On the other hand, as shown the blue plots in Fig. 5a, the $BiVO_4$ photoanode is first tested for 2 h in KBi + Fe(III) for the growth of FeOOH/$BiVO_4$, during which the OER activity decreases in the first half hour but increase gradually to a plateau at 1.5 h. After 2 h, the photoanode is removed from the PEC cell and cleaned with DI water to remove Fe(III) from the surface and then tested in KBi. The current densities decrease slowly to 1.73 mA/cm^2 and it is better than that of pristine $BiVO_4$ (1.29 mA/cm^2) due to the *in situ* formation of FeOOH on the surface of $BiVO_4$ (FeOOH/$BiVO_4$) photoanode. Owing to the dominant dissolution rate, the activity and photo-response of FeOOH/$BiVO_4$ decreases subsequently leading to deteriorated PEC performance [58].

A convenient technique to simultaneously boost the reaction kinetics and stability of the $BiVO_4$ photoanode is designed by adding Fe(III) ions into the electrolyte. The *in situ* generation of the FeOOH co-catalyst on the $BiVO_4$ (FeOOH/$BiVO_4$) photoanode is achieved by the dynamic changes in KBi + Fe(III) during OER. The FeOOH overlayer on the $BiVO_4$ photoanode turns into a hole transfer layer on account of the hole attraction ability of Fe, which can reduce the free energy barriers and accelerate the reaction kinetics. As a result, the current density of the $BiVO_4$ photoanode increases to 2.21 mA/cm^2 at 1.23 V *vs.* RHE, which is much higher than that of the pristine $BiVO_4$ photoanode (1.29 mA/cm^2). Moreover, the $BiVO_4$/FeOOH photoanode shows excellent stability as a result of the inhibition of photo-corrosion rendered by FeOOH. The results demonstrate that changing the microenvironment by the addition of transition metal ions is a facile and promising strategy to enhance the PEC performance and boost the stability of the $BiVO_4$ photoanode. This approach opens a new avenue for the multifunctional modification of photoanodes for efficient solar conversion.

Declaration of competing interest

The authors declare that they have no known competing financial interests or personal relationships that could have appeared to influence the work reported in this paper.

CRediT authorship contribution statement

Hailang Deng: Writing – original draft, Methodology, Investigation, Conceptualization. **Abebe Reda Woldu:** Writing – review

& editing, Formal analysis. **Abdul Qayum:** Methodology, Investigation. **Zanling Huang:** Validation, Formal analysis, Data curation. **Weiwei Zhu:** Writing – review & editing, Visualization, Software, Funding acquisition, Formal analysis, Data curation. **Xiang Peng:** Visualization, Software, Formal analysis. **Paul K. Chu:** Writing – review & editing, Visualization, Funding acquisition. **Liangsheng Hu:** Writing – review & editing, Visualization, Supervision, Resources, Project administration, Investigation, Funding acquisition, Data curation, Conceptualization.

Acknowledgments

This work was financially supported by the Guangdong Basic and Applied Basic Research Foundation (No. 2022A1515110212), the Special Fund Project for Science and Technology Innovation Strategy of Guangdong Province (Nos. STKJ202209077, STKJ202209083, and STKJ202209021), Scientific Research Foundation of Shantou University (No. NTF21022), and City University of Hong Kong Strategic Research Grant (SRG) (No. 7005505).

Supplementary materials

Supplementary material associated with this article can be found, in the online version, at doi:10.1016/j.cclet.2024.109892.

References

[1] B. Zhang, S. Yu, Y. Dai, et al., Nat. Commun. 12 (2021) 6969.
[2] J.H. Kim, D. Hansora, P. Sharma, et al., Chem. Soc. Rev. 48 (2019) 1908–1971.
[3] S. Zhao, B. Liu, G. Zhang, et al., Trans. Tianjin Univ. 29 (2023) 473–481.
[4] J. Zhu, L. Hu, P. Zhao, et al., Chem. Rev. 120 (2020) 851–918.
[5] H. Sun, C.W. Tung, Y. Qiu, et al., J. Am. Chem. Soc. 144 (2021) 1174–1186.
[6] Y. Xiao, C. Feng, J. Fu, et al., Nat. Catal. 3 (2020) 932–940.
[7] R.T. Gao, N.T. Nguyen, T. Nakajima, et al., Sci. Adv. 9 (2023) eade4589.
[8] R.T. Gao, L. Liu, Y. Li, et al., Proc. Natl. Acad. Sci. U. S. A. 120 (2023) e2300493120.
[9] T.W. Kim, K.S. Choi, Science 343 (2014) 990–994.
[10] Y. Kuang, Q. Jia, G. Ma, et al., Nat. Energy 2 (2016) 16191.
[11] D.K. Lee, K.S. Choi, Nat. Energy 3 (2018) 53–60.
[12] D. Lee, W. Wang, C. Zhou, et al., Nat. Energy 6 (2021) 287–294.
[13] J. Huang, Y. Wang, K. Chen, et al., Chin. Chem. Lett. 33 (2022) 2060–2064.
[14] L. Wang, X. Shi, Y. Jia, et al., Chin. Chem. Lett. 32 (2021) 1869–1878.
[15] B. Liu, X. Wang, Y. Zhang, et al., Angew. Chem. Int. Ed. 62 (2023) e202217346.
[16] R.T. Gao, L. Wang, Angew. Chem. Int. Ed. 59 (2020) 23094–23099.
[17] F.M. Toma, J.K. Cooper, V. Kunzelmann, et al., Nat. Commun. 7 (2016) 12012.
[18] R. Lei, Y. Tang, W. Qiu, et al., Nano Lett. 23 (2023) 11785–11792.
[19] Y. Shi, Y. Yu, Y. Yu, et al., ACS Energy Lett. 3 (2018) 1648–1654.
[20] Q. Shi, S. Murcia-López, P. Tang, et al., ACS Catal. 8 (2018) 3331–3342.
[21] J. Eichhorn, S.E. Reyes-Lillo, S. Roychoudhury, et al., Small 16 (2020) 2001600.
[22] S. Wang, G. Liu, L. Wang, Chem. Rev. 119 (2019) 5192–5247.
[23] C. Zhou, S. Wang, Z. Zhao, et al., Adv. Funct. Mater. 28 (2018) 1801214.
[24] L. Jiang, H. Du, L. Li, et al., Trans. Tianjin Univ. 29 (2023) 462–472.
[25] W. Wang, P.J. Strohbeen, D. Lee, et al., Chem. Mater. 32 (2020) 2899–2909.
[26] S. Wang, T. He, P. Chen, et al., Adv. Mater. 32 (2020) 2001385.
[27] D. Kong, J. Qi, D. Liu, et al., Trans. Tianjin Univ. 25 (2019) 340–347.
[28] X. Wang, Chem. Mater. 33 (2021) 6251–6268.
[29] Y. Zhang, L. Xu, B. Liu, et al., ACS Catal. 13 (2023) 5938–5948.
[30] J.B. Pan, B.H. Wang, S. Shen, et al., Angew. Chem. Int. Ed. 62 (2023) e202307246.
[31] M.A. Gaikwad, U.V. Ghorpade, U.P. Suryawanshi, et al., ACS Appl. Mater. Interfaces 15 (2023) 21123–21133.
[32] B. Zhang, X. Huang, Y. Zhang, et al., Angew. Chem. Int. Ed. 59 (2020) 18990–18995.
[33] B. Zhang, L. Wang, Y. Zhang, et al., Angew. Chem. Int. Ed. 57 (2018) 2248–2252.
[34] A.M. Hilbrands, S. Zhang, C. Zhou, et al., J. Am. Chem. Soc. 145 (2023) 23639–23650.
[35] H. Du, J. Fan, C. Miao, et al., Trans. Tianjin Univ. 27 (2021) 24–41.
[36] W. Zhang, J. Ma, L. Xiong, et al., ACS Appl. Energy Mater. 3 (2020) 5927–5936.
[37] N. Clament Sagaya Selvam, S.J. Kwak, G.H. Choi, et al., ACS Energy Lett. 6 (2021) 4345–4354.
[38] S. Anantharaj, S. Kundu, S. Noda, Nano Energy 80 (2021) 105514.
[39] S. Lee, L. Bai, X. Hu, Angew. Chem. Int. Ed. 59 (2020) 8072–8077.
[40] Z. Huang, S. Zhu, Y. Duan, et al., J. Energy Chem. 89 (2024) 99–109.
[41] Z. Huang, A.Reda Woldu, X. Peng, et al., Chem. Eng. J. 477 (2023) 147155.
[42] F. Yang, M. Lopez Luna, F.T. Haase, et al., J. Am. Chem. Soc. 145 (2023) 21465–21474.
[43] C. Kuai, C. Xi, A. Hu, et al., J. Am. Chem. Soc. 143 (2021) 18519–18526.
[44] Q. Sun, K. Ren, L. Qi, ACS Appl. Mater. Interfaces 14 (2022) 37833–37842.
[45] G. Fang, Z. Liu, C. Han, et al., ACS Appl. Energy Mater. 4 (2021) 3842–3850.
[46] S. Chen, B. Li, D. Huang, et al., ACS Appl. Mater. Interfaces 13 (2021) 17586–17598.
[47] R.T. Gao, J. Zhang, T. Nakajima, et al., Nat. Commun. 14 (2023) 2640.
[48] H. Duan, H. Wu, H. Zhong, et al., J. Phys. Chem. C 126 (2022) 7688–7695.
[49] H. Wu, S. Qu, Z. Xie, et al., ACS Appl. Energy Mater. 5 (2022) 8419–8427.
[50] Q. Wang, L. Wu, Z. Zhang, et al., ACS Appl. Mater. Interfaces 14 (2022) 26642–26652.
[51] R.T. Gao, D. He, L. Wu, et al., Angew. Chem. Int. Ed. 59 (2020) 6213–6218.
[52] Z. Wang, Y. Guo, M. Liu, et al., Adv. Mater. 34 (2022) e2201594.
[53] W. Fang, L. Fu, A. Qin, et al., ACS Appl. Energy Mater. 5 (2022) 6313–6323.
[54] T. Zhou, S. Chen, J. Wang, et al., Chem. Eng. J. 403 (2021) 126350.
[55] M. Pradhan, S. Maji, A.K. Sinha, et al., J. Mater. Chem. A 3 (2015) 10254–10257.
[56] Y. Hu, J. Zhou, L. Li, et al., J. Mater. Chem. A 10 (2022) 602–610.
[57] X. Xiong, C. Zhang, X. Zhang, et al., Electrochim. Acta 389 (2021) 138795.
[58] G. Zhang, Z. Li, J. Zeng, et al., Appl. Catal. B: Environ. 319 (2022) 121921.